

Local seismicity around the Chain Transform Fault at the Mid-Atlantic Ridge from OBS observations

David Schlaphorst¹, Catherine Rychert², Nicholas Harmon², Stephen Hicks³, Petros Bogiatzis², John Michael Kendall⁴, and Rachel Abercrombie⁵

¹University of Lisbon

²University of Southampton

³Imperial College London

⁴University of Oxford

⁵Boston University

November 21, 2022

Abstract

Seismicity along transform faults provides important constraints for our understanding of the factors that control earthquake ruptures. Oceanic transform faults are particularly useful due to their relatively simple structure in comparison to continental counterparts. The seismicity of several fast-moving transform faults has been investigated by local networks, but as of today there have not been many studies of slower spreading centres. Here we present the first local seismicity catalogue based on event data recorded by a temporary broadband network of 39 ocean bottom seismometers located around the slow-moving Chain Transform Fault (CTF) along the Mid-Atlantic Ridge (MAR) from March 2016 to March 2017. Locations are constrained by simultaneously inverting for a 1-D velocity model informed by the event P- and S-arrival times. Depths and focal mechanisms of the larger events are refined using deviatoric moment tensor inversion. We find a total of 972 events in the area. Most of the seismicity is located at the CTF (700) and Romanche transform fault (94) and the MAR (155); a smaller number (23) can be observed on the continuing fracture zones or in intraplate locations. The ridge events are characterised by normal faulting and most of the transform events are characterised by strike slip faulting, but with several reverse mechanisms that are likely related to transpressional stresses in the region. CTF events range in magnitude from 1.1 to 5.6 with a magnitude of completeness around 2.3. Along the CTF we calculate a b-value of 0.81 ± 0.09 . The event depths are mostly shallower than 15 km below sea level (523), but a small number of high-quality earthquakes (16) are located deeper, with some (8) located deeper than the brittle-ductile transition as predicted by the 600°C-isotherm from a simple thermal model. The deeper events could be explained by the control of seawater infiltration on the brittle failure limit.

Hosted file

supplementary_figures_v3.docx available at <https://authorea.com/users/527361/articles/596623-local-seismicity-around-the-chain-transform-fault-at-the-mid-atlantic-ridge-from-obs-observations>

1 Local seismicity around the Chain Transform Fault at the
2 Mid-Atlantic Ridge from OBS observations

3

4 David Schlaphorst^{1,2*}, Catherine A. Rychert³, Nicholas Harmon³, Stephen P. Hicks⁴, Petros
5 Bogiatzis³, J-Michael Kendall⁵, Rachel E. Abercrombie⁶

6

7 (*corresponding author: dschlaphorst@fc.ul.pt)

8

9 ¹ Instituto Dom Luiz (IDL), Faculdade de Ciências, Universidade de Lisboa, Campo Grande,
10 1749-016 Lisboa, Portugal.

11 ² School of Earth Sciences, University of Bristol, Wills Memorial Building, Queens Road,
12 Bristol BS8 1RJ, UK.

13 ³ Ocean and Earth Science, University of Southampton, National Oceanography Centre,
14 Southampton, UK

15 ⁴ Department of Earth Science and Engineering, Imperial College London, UK.

16 ⁵ Department of Earth Sciences, University of Oxford, UK.

17 ⁶ Department of Earth & Environment, Boston University, USA.

18

19 **Summary**

20 Seismicity along transform faults provides important constraints for our understanding of the
21 factors that control earthquake ruptures. Oceanic transform faults are particularly useful due
22 to their relatively simple structure in comparison to continental counterparts. The seismicity
23 of several fast-moving transform faults has been investigated by local networks, but as of
24 today there have not been many studies of slower spreading centres. Here we present the first
25 local seismicity catalogue based on event data recorded by a temporary broadband network of
26 39 ocean bottom seismometers located around the slow-moving Chain Transform Fault
27 (CTF) along the Mid-Atlantic Ridge (MAR) from March 2016 to March 2017. Locations are
28 constrained by simultaneously inverting for a 1-D velocity model informed by the event P-
29 and S-arrival times. Depths and focal mechanisms of the larger events are refined using
30 deviatoric moment tensor inversion. We find a total of 972 events in the area. Most of the
31 seismicity is located at the CTF (700) and Romanche transform fault (94) and the MAR
32 (155); a smaller number (23) can be observed on the continuing fracture zones or in intraplate
33 locations. The ridge events are characterised by normal faulting and most of the transform
34 events are characterised by strike slip faulting, but with several reverse mechanisms that are
35 likely related to transpressional stresses in the region. CTF events range in magnitude from
36 1.1 to 5.6 with a magnitude of completeness around 2.3. Along the CTF we calculate a *b*-
37 value of 0.81 ± 0.09 . The event depths are mostly shallower than 15 km below sea level
38 (523), but a small number of high-quality earthquakes (16) are located deeper, with some (8)
39 located deeper than the brittle-ductile transition as predicted by the 600°C-isotherm from a
40 simple thermal model. The deeper events could be explained by the control of seawater
41 infiltration on the brittle failure limit.

42

43 **Introduction**

44

45 The factors that dictate the location, size and style of earthquake faulting are fundamental for
46 our understanding of hazard and hazard mitigation (e.g., Slemmons et al., 1986). Oceanic
47 transform faults (OTF), such as those that connect the many fragmented sections of the slow
48 spreading Mid-Atlantic Ridge, are an ideal place to investigate the earthquake cycle. While
49 not a great risk to humans themselves due to their often remote locations, OTFs are thought
50 to be relatively simple in terms of thermal structure, fault zone geometry, slip rate and
51 rheology in comparison to more hazardous continental counterparts such as the San Andreas
52 fault. Therefore, the study of earthquakes around OTFs provides important constraints to
53 inform hazard assessments in continental areas. Ocean lithosphere is characterised by
54 relatively homogenous composition, with mafic to ultra-mafic lithologies. In addition,
55 deformation tends to be localised in a narrow zone, roughly 20 to 30 km wide (Fox & Gallo
56 1984) with nearly vertically oriented faults on which total motions should roughly correspond
57 to ridge spreading rates. Finally, the region of potential seismic slip is also well-predicted by
58 the region shallower than the 600°C isotherm predicted by simple thermal models such as the
59 halfspace cooling model (e.g., Abercrombie & Ekström, 2001).

60

61 However, a vast majority of events cannot be detected around OTFs, due to their general
62 inaccessibility. Being in the middle of the ocean, the closest landmasses and, thus, seismic
63 land stations are often located at teleseismic distances. Previous studies have used teleseismic
64 data to investigate earthquake sources along OTFs (e.g., Engeln et al., 1986; Bergman &
65 Solomon, 1988; Abercrombie & Ekström, 2001). However, smaller events are not recorded
66 teleseismically, and the magnitude of completeness offered by global monitoring networks is
67 high. In particular, this affects the observation of microseismicity around the brittle-ductile

68 transition. Furthermore, the use of a non-local velocity model can influence the accuracy of
69 hypocentre depth localisations.

70

71 Over the last decade the installation of dense ocean bottom seismometer (OBS) networks has
72 enabled the more detailed study of local seismicity along Pacific OTFs, e.g., at the Discovery
73 OTF (McGuirre et al., 2012) or the Blanco OTF (Kuna et al., 2019). However, spreading
74 rates in the Pacific are mostly classified as intermediate or even fast (> 60 mm/yr), whereas
75 the MAR is a slow-spreading ridge, which could have an effect on the local seismicity. The
76 Chain and Romanche, as well as other OTFs in the North Atlantic are constructed of very
77 thin, highly serpentinized crust (Detrick et al., 1993) and teleseismic earthquakes can be
78 observed in the shallow mantle beneath (Abercrombie & Ekström, 2001). While there have
79 been studies using OBS networks to investigate ridge segments or ridge-transform
80 intersections in the Atlantic (e.g., Toomey et al., 1985; Grevemeyer et al., 2013, Gregory et
81 al., 2021; Yu et al., 2021), local studies of Atlantic OTFs have been sparse.

82

83 From March 2016 to March 2017, a temporary network of 39 seismic ocean bottom
84 seismometers (OBS) was deployed around the Chain transform fault (CTF) on the MAR and
85 continuing eastward fracture zone (FZ) as part of the PI-LAB (“Passive Imaging of the
86 Lithosphere-Asthenosphere Boundary”) project and EURO-LAB (Experiment to Unearth the
87 Rheological Oceanic Lithosphere-Asthenosphere Boundary) (Fig. 1; Agius et al., 2018, 2021;
88 Harmon et al., 2018, 2020, 2021; Hicks et al., 2020; Bogiatzis et al., 2020; Wang et al., 2020;
89 Rychert et al., 2021; Saikia et al., 2020, 2021; Leptokaropoulos et al., 2021). The CTF zone has
90 a length of 300 km and varies in thickness between 7 km and 20 km with an African Plate
91 half-spreading rate of 18.2mm/yr and a South American Plate half spreading rate of
92 15.7mm/yr (Demets et al., 1994; Harmon et al., 2018). The aim of the experiment was to

93 cover an area of transition from oceanic crust formation at the MAR to older plate ages away
94 from the ridge; the setup was chosen to facilitate the observation of thickening oceanic
95 lithosphere relative to increasing plate age (Rychert et al., 2021). During the same time, the
96 International Seismic Centre (ISC) recorded 40 earthquakes in the region, of which 23 are
97 located in the vicinity of the Romanche transform fault (RTF), 7 close to the CTF and 8
98 around the MAR; 2 earthquakes were found on the inactive part of the Chain FZ.

99

100 In this study, we present the first catalogue of local seismicity around the equatorial MAR
101 near the CTF, together with a 1D velocity model of the oceanic crust and upper mantle. The
102 catalogue provides event times, hypocentre locations and magnitude information. We
103 investigate small-scale seismicity variations along the CTF, the adjacent Chain FZ and the
104 adjoining sections of the MAR. We also compute earthquake-magnitude distribution at CTF
105 and RTF. Furthermore, we investigate the seismicity in relation to the depth of the brittle
106 ductile region predicted by simple thermal models.

107

108 **Method**

109

110 *Localisation*

111

112 The data were recorded by the 39 PI-LAB OBS stations during their one-year deployment
113 (Fig. 1, Table 1). The stations are mostly distributed in two lines north and south of the CTF
114 and eastern FZ continuation with an average spacing of 40 km around the active part. On the
115 CTF, the typical minimum station distance to the events is around 50 km. We use a
116 Butterworth bandpass filter with corner frequencies of 4Hz and 18Hz, which enhances the
117 signal-to-noise ratio in a marine environment using OBS instruments. The a priori temporary

118 set of picks is created using automated picks from a short-time average divided by long time
119 average (STA/LTA) detector. We use a 1D velocity model that is based on CRUST1.0
120 (Laske et al., 2012), which includes an average regional crustal thickness of around 8 km
121 (Fig. 2A), plus a 2.90 km thick water layer, which corresponds to the depth of the shallowest
122 OBS location (S11D). Deeper than 35km, it is based on ak135 (Kennett et al., 1995). Here,
123 ST and LT time windows of 0.2s and 10s are used, together with thresholds of 4 (trigger on)
124 and 1.5 (trigger off). This results in 1492 a priori events with 11399 P- and 13948 S-picks.

125

126 The P- and S- picks are refined manually and iteratively in combination with an update on the
127 1-D velocity model and the event locations. Event locations are computed using the
128 NonLinLoc package (Lomax et al., 2000). The package performs a probabilistic, non-linear
129 global-search inversion using the list of picked arrival times and a regional velocity model as
130 input. Following the probabilistic approach of Tarantola & Valette (1982) it calculates the
131 hypocentre location using the maximum likelihood of a probability density function of model
132 parameters in the temporal and spatial domain. The velocity model is updated using
133 VELEST3.1 (Kissling et al., 1994), which simultaneously inverts for 1-D P- and S-wave
134 velocities and hypocentral parameters. The velocity model has a substantial influence on the
135 depth accuracy, whereas lateral localisation of most earthquakes can be constrained even if
136 more general models are used. Further details can be found in Appendix 1.

137

138 Given this we perform an additional test to verify the robustness of the depth estimates. We
139 compare NonLinLoc solutions with different maximum search depth limits (15, 20, 25, 30
140 km, as well 200 km, which we will label as “no limit”). We use the following steps to
141 establish the preferred solution from the NonLinLoc testing with different maximum search
142 depth limits. Although the lateral locations are typically the same regardless of the depth

143 limit, we eliminate the few solutions where the lateral location of the event lies outside of
144 error of the rest of the locations (Fig. S1). We then choose the location that has the lowest
145 root mean square (RMS) error if it is outside of error from the remaining location solutions
146 (see Suppl. Fig. S1). For locations where results using multiple depth cut-offs are within error
147 of each other and shallower than 30 km we use the solution with the lowest RMS error. In
148 cases where the lowest RMS error is reached at > 30 km depth from the sea surface and the
149 solution is within error of a shallower solution, we favour a shallower solution, but we mark
150 the quality as marginal. We use 30 km depth as a cut-off because it corresponds to the
151 approximate depth of the 900 – 1000 ° isotherms from thermal models, which may be the
152 limit of predicted brittle deformation (Molnar, 2020; Kohli et al., 2021). Although locations
153 deeper than 30 km are generally unlikely, we will also present the deep solutions since deeper
154 hypocentres have been found in other locations (McGuire et al., 2012; Kuna et al., 2019; Yu
155 et al., 2021). To ensure the robustness of the computed depths are unbiased by
156 heterogeneities due to long raypaths, we also carried out tests using only the data from the
157 closest five stations with which an azimuthal gap below 180 degrees was still maintained. We
158 did this on a random sampling of 6 events ranging from M_L of 3.3 to 5.6. The locations
159 excluding longer paths were all within error of the original results.

160

161 For larger events, it is possible to carry out full moment tensor (MT) inversions, which gives
162 additional constraints on the depth accuracy (e.g., Braunmiller & Nábělek, 2008). We use the
163 Grond software tool (Heimann et al., 2018), which carries out a Bayesian bootstrap-based
164 inversion of the time-domain deviatoric MT. The data is filtered between 12.5 s and 25 s. For
165 solution stability reasons we focus on the depth location while keeping the previously
166 determined latitude and longitude information fixed. Our tests show that in general the same
167 epicentral locations are found within uncertainties. We estimate the quality of these

168 measurements based on the following parameters (Suppl. Figs. S2, S3): 1) the number of
169 stations for which the theoretical waveforms fit the data is high, we assign quality level “MT
170 best”, respectively. If the fit is generally poorer and/or the number of stations with good fits
171 is low, we categorise the event as “MT fair”. 2) The agreement of stacked radiation patterns
172 from different ensembles of stations (good agreement for best, overall agreement with
173 potential outliers for fair). All solutions show a depth constraint that is well defined. In all
174 cases where an MT solution exists, we use this depth estimate.

175

176 *Magnitudes*

177

178 We calculate local magnitudes for all the located earthquakes using amplitude measurements
179 of the picked P-arrivals. After demeaning and detrending the data, we remove the instrument
180 response and simulate the response of a Wood-Anderson seismometer. The data are then
181 filtered using a high-pass filter with a corner frequency of 4Hz to reduce oceanic noise. To
182 account for further noise we introduce a signal-to-noise threshold of 1.3 for the zero-to-peak
183 amplitude calculations that are used to compute local magnitudes. To account for changes in
184 recorded amplitude with hypocentral distance due to geometric spreading and anelastic
185 attenuation the event magnitudes are adjusted using the correction term:

186

$$187 \text{Log}_{10}(A) - M_{ISC} = -1.46 \text{Log}_{10}(r/100) - 0.0016 (r - 100) - 6.2$$

188

189 Here, A is the recorded amplitude, M_{ISC} is the magnitude as derived by the International
190 Seismological Centre (ISC), and r is the hypocentral distance. The term is derived similarly
191 to Abercrombie et al. (1996), using an empirical comparison to our MT solutions (Fig. 3).

192

193 *Magnitude-earthquake distribution*

194

195 The earthquake magnitude distribution can be described by the b -value, which is the gradient
196 of the Gutenberg-Richter relationship ($\text{Log}\{N(M)\} = a - bM$; Gutenberg & Richter, 1944).

197 The relationship shows that the number of events (N) above a certain magnitude (M) can be
198 expressed by two positive constants, representing the overall seismic activity (a) and the
199 relative occurrence of small to large magnitude earthquakes (b).

200

201 To calculate the associated uncertainties we perform the maximum likelihood method (Aki
202 1965; Utsu 1965; Bender 1983) in combination with a Kolmogorov-Smirnov test. The
203 magnitude of completeness, M_C , is truncate at $M_c = 2.3$ to avoid large variations since they
204 can bias the results using a maximum likelihood calculation. The solution is accepted if the
205 magnitude distribution and the straight-line gradient b reach a similarity above M_C above a
206 predetermined significance level, in our case chosen to be more rigorous at 20% (Schlaphorst
207 et al., 2016).

208

209 **Results**

210

211 In total, 972 earthquakes could be located laterally (Fig. 4). Constraining depths with a larger
212 network spacing of around 40 km poses challenges in this setting. Still, we were able to
213 constrain depths for 928 events. 118 could be constrained by applying an MT inversion (Fig.
214 4B). Of the remaining event locations 650 are classified as good (Fig. 4C) and 150 are
215 classified marginal quality (Fig. 4D). The majority of the MT constrained events (88) are
216 located on the CTF and FZ. The lateral location uncertainty is smaller than depth uncertainty
217 with a median value of $\tilde{y} = 2.86$. Moment tensor solutions show the lowest depth

218 uncertainties with median values of $\tilde{z} = 5.42$ km in comparison with the median NonLinLoc
219 solutions for good ($\tilde{z} = 7.96$ km) and marginal ($\tilde{z} = 11.87$ km) categories (Fig. 4B, C, D).
220 NonLinLoc hypocentres are better constrained inside the network with the following median
221 values of $\tilde{y} = 2.39$ km and $\tilde{z} = 8.36$ km for CTF and $\tilde{y} = 15.09$ km and $\tilde{z} = 24.81$ km for RTF.
222 Nearly all of the events are found on or close to the OTFs (793) and the MAR (155). Only a
223 small number (10) are located on the inactive continuing FZs. Another 13 can be found off
224 these features. Of the events located on or close to an OTF, 700 are close to the CTF, of
225 which the majority is concentrated towards the eastern side, particularly clustered towards the
226 ridge-transform intersection. A further 94 can be found around the RTF.

227

228 Earthquake depths, relative to sea level, determined from NonLinLoc, range from the
229 seafloor to 43 km depth beneath the sea surface. Most (716) are located shallower than 15
230 km. Events on the MAR, away from the ridge-transform intersection, are mostly (36 out of
231 46) shallower than 10 km. Events on the MAR near the transform are deeper, with 12 events
232 between 15 km and 30 km categorized as good. 60 events in the entire catalogue were located
233 between 30 and 40 km depth, only 4 of which are classified as good and 56 as marginal. 14
234 are located at depths greater than 40 km and all categorised as marginal (Fig. 4D).

235

236 Most of the MT depths are well-constrained (96 out of 118; Fig. 5; Suppl. Figs. 2, 3). Most
237 solutions (63) are characterised by probability density functions (pdfs) with a clear singular
238 peak. Some solutions (35) have a more complex distribution, but the dominant peak is
239 shallow (<20 km). We find 20 events where a deep (20 – 49 km) MT solution exists that fits
240 the waveforms equally well or better than a shallower solution (<20 km) that we present for
241 completeness (Fig. 6). The deep solutions are likely unrealistic, given the expected maximum
242 depth of brittle deformation (Molnar, 2020; Kohli et al., 2021). Therefore, we favour the

243 shallower solution. In general, the deepest events are located along the CTF and RTF, while
244 the events beneath the MAR are shallower than 12 km below sea level. There is only one
245 event on the MAR that is deeper than 12 km. There is one intraplate earthquake with an MT
246 solution located on the African plate near the Chain FZ, with a depth of 18 km.
247
248 MT inversion of 118 events in our catalogue shows a mix of strike slip, normal and reverse
249 faults across the region (Fig. 5). Of the 88 focal mechanisms located on the CTF, the majority
250 shows right lateral strike-slip movement (39), mostly dipping to the north. Towards the
251 eastern end of the CTF, a combination of strike-slip and reverse faulting is observed (18).
252 Several reverse faulting mechanisms can be observed in some locations along the CTF as
253 well (20). Nearly all of the 29 MAR events show predominantly normal fault mechanisms
254 with a minor strike-slip component in some cases. Furthermore, a rotation of the normal
255 faulting axis can be observed close to ridge-transform intersections (Fig. 5; Suppl. Fig. S6).
256 The one intraplate event on the Chain FZ has a moment tensor which shows normal faulting
257 with fault plane solutions with north-south strike orientations
258
259 The local magnitudes from our catalogue range from 1.1 to 6.2. The local 6.2 magnitude is a
260 clipped estimate of the Romanche event, that was a larger M_w 7.1 in the global CMT
261 (Dziewonski et al., 1981; Ekström et al., 2012;) and in a detailed local study of the event
262 (Hicks et al., 2020). The local magnitude scale clips on this large event since it is outside of
263 our array with a small backazimuthal coverage. The next largest event in the catalogue is a
264 M_L 5.6 located on the CTF. We note that our relationship between amplitude and local
265 magnitude scale (Fig. 3) resembles one derived for the Azores (Gongóra et al., 2004), but
266 also to the continental setting of southern California (Hutton & Boore, 1987).
267

268 The moment magnitudes from MT inversion range from 3.0 to 6.2. This largest magnitude
269 corresponds to the M_w 7.1 Romanche event (Hicks et al., 2020). The magnitude is vastly
270 underestimated for three main reasons: 1) the large azimuthal gap, 2) the distance to the
271 network, and 3) the usage of a CTF based velocity model and magnitude calibration. On the
272 CTF three $M_w > 5$ events were located, the largest being a M_w 5.6. The largest earthquake that
273 we recorded on a MAR segment was a M_w 4.5, while the largest intraplate earthquake we
274 recorded was a M_w 3.2.

275

276 The b -value for the CTF is 0.81 ± 0.09 and for the RTF is 0.76 ± 0.22 . The network
277 configuration results in large distances to the stations and azimuthal gaps for the events at the
278 RTF, which leads to magnitude estimations being less well constrained. These factors
279 combined with the lower number of detected events leads to higher uncertainties for events at
280 RTF. In addition, the magnitude of completeness is larger outside the network at the RTF
281 ($M_C = 3.4$) compared to inside the network at CTF ($M_C = 2.3$). The RTF also has larger
282 median local magnitudes ($M_L = 3.7$) compared to the CTF ($M_L = 2.4$). Within the CTF the
283 median local M_L values vary, with $M_L = 2.5$ in the west and $M_L = 2.3$ in the east.

284

285

286 **Discussion**

287

288 The results generally show an expected pattern of event distribution. They are mostly located
289 close to the ridge-transform plate tectonic boundary between the African and South American
290 Plates. The sub-ridge events are located at depths shallower than 12 km beneath sea level.
291 These likely occur in the crust and the uppermost mantle assuming around 3 km average
292 water depth at the ridge and a 6-7 km average crustal thickness (Christeson et al., 2019).

293 These can be explained through extension of the crust due to seafloor spreading. Earthquakes
294 at slightly deeper depths than the crust beneath the ridge may occur given that geodynamic
295 modelling suggests that lateral conductive cooling results in non-negligible thickness of the
296 mantle lithosphere at slow spreading centres (Parmentier & Morgan, 1990). The deeper
297 earthquakes observed in the transforms suggest that there is brittle deformation to deeper
298 depths than beneath the ridges. The strain rate can be another component in controlling the
299 depth extent of seismicity (Molnar, 2020). A deeper brittle-ductile transition beneath the
300 transform in comparison to the ridges is predicted by simple thermal models. Brittle
301 deformation in the mantle lithosphere has also been observed in teleseismic estimates for
302 CTF and RTF (Abercrombie & Ekström, 2001).

303

304 The focal mechanisms along the plate boundary are also generally consistent with the ridge-
305 transform system in the region. Specifically, we observed mostly normal fault MT solutions
306 near the MAR segments, and mostly strike-slip solutions along the CTF and RTF consistent
307 with the global view from the global CMT (Dziewonski et al., 1981; Ekström et al., 2012).

308 The general pattern of north dipping focal mechanisms on the CTF is in agreement with
309 previous results that are based solely on teleseismic observations (Abercrombie & Ekström,
310 2001). At the ridge-transform intersection we observe the rotation of the strike of the normal
311 fault focal mechanism from ridge parallel on the ridge towards the strike direction of the
312 OTF. This rotation reflects the transition in stress regime as the plate boundary transitions
313 from spreading to transform fault tectonics (Fox and Gallo, 1984) as predicted by
314 geodynamic modelling (Morgan & Parmentier, 1984). This also results in the observed
315 arcuate shaped scarps bending in towards the transform faults in the ridge-transform
316 intersection in the CTF (Harmon et al. 2018).

317

318 The presence of reverse fault MT solutions in some parts of the CTF is indicative of
319 transpression in the strike slip system. The reverse fault mechanisms are typically associated
320 with topographic highs within the CTF, which have been interpreted as positive flower
321 structures associated with restraining bends in the normal fault system (Harmon et al., 2018).
322 The four positive flower structures have visible sharp scarps in the bathymetry (Harmon et
323 al., 2018), and taken with the MT solutions, suggests that these are active features and the
324 CTF is in active transpression today. Transpression could be caused by a present-day rotation
325 and re-adjustment of the African-South American spreading system. Previously, it has been
326 suggested that the relative plate motions in the region have undergone a rotation of $\sim 11^\circ$
327 anticlockwise based on observations of transpressional features on the major FZs to the north,
328 for example Romanche and St. Paul, (Bonatti et al., 1994; Maia et al., 2016). Our
329 observations support these notions and suggest that the change in motions is ongoing.

330

331 The cluster of intraplate seismicity (5 events) observed on the Chain FZ on the African Plate
332 at -11.5° longitude suggests there are internal stresses in the region of the earthquakes. The
333 MT solution indicates a relatively deep event (18 km) suggesting strain is accumulating in the
334 deeper part of the lithosphere caused brittle deformation there. The near vertical (or
335 horizontal) fault plane and north-south strike direction are at odds with the expected tectonic
336 fabric of the roughly east-west trending Chain FZ, so it does not appear to be re-activation of
337 the FZ. Another example of a large intraplate oceanic earthquake in the Wharton Basin in the
338 Indian Ocean was interpreted as FZ reactivation given that MT solutions were consistent with
339 the FZ orientations (Yue et al., 2012), and the event may have been related to the nearby
340 Sumatran subduction zone. One explanation for our event is that the intraplate stresses are
341 due to the aforementioned rotation of the relative plate motions (Bonatti et al., 1994; Maia et
342 al., 2016). However, it is unclear whether the observed focal mechanism would be consistent

343 with this interpretation. Another potential explanation of intraplate stress in the region may
344 be due to ocean mantle dynamics. Surface wave tomography and magnetotelluric imaging
345 across the PI-LAB region image a high velocity and high resistivity in this region centred at
346 10.5°W longitude and 0°N latitude with shear velocities of greater than 4.4 km/s and \log_{10}
347 (resistivities) > 1.5 extending from 30 to 100 km depth that was interpreted as a lithospheric
348 drip (Harmon et al., 2020; 2021; Wang et al., 2020). The lack of an observed receiver
349 function phase from the lithosphere-asthenosphere boundary in this location was interpreted
350 as either the absence of melt ponding beneath the plate and/or strong lithosphere-
351 asthenosphere topography, again consistent with a drip (Rychert et al., 2021). The observed
352 vertical MT motion of the large event recorded in this region may be consistent with the
353 vertical stresses of the downwelling lithosphere (Fig. 5).

354

355 Events beneath the CTF are located deeper than the predicted depth of the 600°C isotherm
356 from half-space cooling, i.e., a greater depth than the previously proposed limit of seismic
357 slip at 600°C based on teleseismic observations (Abercrombie & Ekström, 2001) and
358 earthquake rupture experiments (Boettcher et al., 2007). Earthquakes deeper than expected
359 based on isotherms predicted for an oceanic transform from the half space cooling model
360 have also been observed at Blanco (Kuna et al., 2019), Gofar (McGuire et al., 2012) and
361 Romanche (Yu et al., 2021). These observations are typically interpreted as lithospheric
362 cooling caused by hydrothermal circulation, which can deepen the depth of the brittle-ductile
363 transition (Roland et al., 2010). In some cases, the events were deeper than expected by
364 numerical modelling accounting for hydrothermal circulation (Roland et al., 2010; McGuire
365 et al., 2012; Kuna et al., 2019). Therefore, an alternative explanation that was suggested
366 based on exhumed hydraulically altered mylonites is that brittle and ductile deformation can
367 occur over a broad range of temperatures (300°C – 900°/1000°C) and, therefore, a broad

368 range of depths, owing to variable seawater infiltration and grain sizes along the fault
369 (Molnar, 2020; Kohli et al., 2021).

370

371 The b -value of the entire catalogue of CTF events is lower than the global average value of
372 1.0 but in agreement with other studies in the region (Leptokaropoulos et al, 2021). The low
373 b -value (0.81 ± 0.09) also supports the notion that average coupling along the CTF is low and
374 that much of the strain is accommodated aseismically. However, historical seismicity, which
375 has resulted in several large events ($M_w > 6.5$), suggests that coupling in discrete locations
376 may be higher (Shi et al., 2021). This agrees with results from Blanco Transform, where
377 crustal b -values are similarly low ($b = 0.78 \pm 10$) and coupling is low but variable along the
378 fault (Kuna et al., 2019).

379

380 We compare the cumulative moment release over the 1-year of our array to examine the
381 average seismic coupling. We find that the cumulative moment release on the CTF was $4.9 \times$
382 10^{17} Nm. The release on the RTF was 5.7×10^{19} Nm. The release on the ridge segments had a
383 cumulative moment of 3.3×10^{16} Nm. The higher release on the Romanche is due to the M_w
384 7.1 event and its aftershock sequence. A more detailed investigation of this event is presented
385 in (Hicks et al., 2020). The predicted moment release per year for the thermal lithosphere
386 from Boettcher and Jordan, (2004) for the CTF is 5.9×10^{18} Nm yr⁻¹, which suggests only
387 ~1% of the predicted moment release was released seismically over the year-long observation
388 period. Our results also support the notion that the CTF is relatively weak and not coupled.
389 For the entire Romanche, the predicted value of cumulative moment release from the thermal
390 lithosphere is 2.9×10^{19} Nm yr⁻¹, approximately half of the observed moment release. Large
391 events like the M_w 7.1 occur relatively rarely, approximately every 30 years on Romanche,
392 indicating the moment release during this time was particularly high. Given that these large

393 events occur on different segments, and do not rupture the entire length of the transform fault,
394 portions of the RTF likely have high seismic coupling. This observation also highlights the
395 temporal variability of moment release on OTFs. The MAR segments show a very low
396 cumulative moment (3.3×10^{16} Nm) compared to the OTFs ($\geq 4.9 \times 10^{17}$ Nm) in the region
397 for the duration of the deployment, which may suggest that the normal faulting also has a low
398 coupling during this time period.

399

400 **Conclusions**

401

402 We present an earthquake catalogue from a broadband ocean bottom seismic experiment
403 from March 2016 to March 2017 at the equatorial MAR centred around the Chain FZ, which
404 provides one of the first detailed seismicity study from a larger local network around a slow
405 moving OTF. Most of the events are located on the South American – African Plate boundary
406 as expected although we also recorded 10 events near the Chain FZ, east of the OTF and 13
407 additional intraplate earthquakes. Focal mechanisms on the MAR are predominantly
408 characterised as normal faulting and on the OTF they are predominantly strike slip as
409 expected. A few (17) predominantly reverse faulting mechanisms on the transform are likely
410 caused by a transpressional stress regime related to current rotation of the ridge-transform
411 system. The focal mechanism of an intraplate event on the FZ shows vertical displacement,
412 consistent with a hypothesized nearby lithospheric drip. The magnitudes range from 1.1 to
413 5.6 and we find a b -value of 0.81 ± 0.09 for the CTF. The earthquakes on the ridge are
414 limited to crust and shallowest mantle (< 12 km depth) while the events on the CTF are
415 deeper, with high quality MT location depths of up to 26 km beneath the sea surface, which is
416 much deeper than the depth of the brittle-ductile transition predicted for simple thermal
417 models. These deeper events are likely linked to the effects of hydrothermal circulation.

418

419 **Acknowledgements**

420 All images were produced using GMT (Wessel et al., 2013). Additional information about
421 SDX can be found at www.liv.ac.uk/~aeh/index.html. D.S. would like to acknowledge the
422 financial support FCT through project UIDB/50019/2020 – IDL.
423 D.S. managed the study and carried out the locating. C.A.R. and N.H. conceived the
424 experiment, acquired funding, managed the project, and contributed to the manuscript. S.P.H.
425 created the initial automated detection of events, assisted with the locations, and commented
426 on the manuscript. P.B. worked on event depth improvements and commented on the
427 manuscript. J.M.K. co-managed the project and commented on the manuscript. R.E.A.
428 contributed to improving the event localization method and commented on the manuscript.

429

430 **Data Availability**

431 The continuous raw seismic waveform data from the PI-LAB OBS network is available to
432 download from IRIS Data Management Center (https://doi.org/10.7914/SN/XS_2016).

433

434 **Appendix 1 – Details on iterative pick refinement, model update and event localisation**
435 **in NonLinLoc**

436 In step 1, P- and S-arrivals are readjusted using the vertical component and the Seismic
437 Analysis Code (SAC). This is done without the implementation of calculated theoretical
438 arrival times derived from the automated picks in order to keep the reassessed picks unbiased.
439 Although different filters as well as the unfiltered data are used to evaluate potential onsets,
440 we use the same corner frequencies to determine the onsets to have consistent P- and S-
441 moveouts and P-to-S travel time differences. The weighting of picks is assigned to reflect
442 their quality, using levels from 0 (highest) to 4 (lowest). The levels are associated with an

443 uncertainty in arrival time, using values of 0.1s, 0.2s, 0.5s, 0.8s, and 1.5s (Hicks et al., 2014).

444 Picks of quality level 4 are subsequently omitted from the locating process.

445

446 In step 2, the event locations are computed using the NonLinLoc package (Lomax et al.,
447 2000). The package performs a probabilistic, non-linear global-search inversion using the list
448 of picked arrival times and a regional velocity model as input. Following the probabilistic
449 approach of Tarantola & Valette (1982) it calculates the hypocentre location using maximum
450 likelihood of a probability density function of model parameters in the temporal and spatial
451 domain. The initial velocity model is given by CRUST1.0 resulting in an average regional
452 crustal thickness of around 8 km (Fig. 2A), plus a 2.90 km thick water layer, which
453 corresponds to the depth of the shallowest OBS location (S11D). We do not include a
454 sediment layer since it is supposed to be very thin in the area (Agius et al., 2018; Saikia et al.,
455 2020). In this step, we also combine picks that are counted as multiple events by the
456 STA/LTA detector, thus reducing the overall number of events.

457

458 A minimum of 3 stations with clearly observable and coherent arrivals is required to identify
459 the event. We use a search grid spacing of 1km in all three dimensions and an average v_P/v_S
460 ratio of 1.73, based on picked P–S arrival time differences (Fig. 2B). The quality of the
461 resulting location is based on temporal uncertainty (i.e., root mean square or RMS error) as
462 well as spatial uncertainty. The latter is a combination of the size of the ellipsoidal
463 approximation to the 1σ confidence level of the location likelihood scatter and the overall
464 shape of the scatter sample. Lateral localisation of most earthquakes can be constrained
465 relatively precisely, even if more general models are used, whereas the velocity model has a
466 larger impact on depth localisation.

467

468 In step 3, the picks of events with low quality are refined. This includes all events that either
469 have large location uncertainty and/or where picks and theoretical arrival times show large
470 mismatches. Here we use the Seismic Data eXplorer (SDX; Hicks et al., 2014), additionally
471 including the two horizontal components and the hydrophone component. SDX updates
472 theoretical onset time calculations of P- and S-phases automatically after each change of pick
473 placement. In general, this reduces the number of mispicks. There are, however, instances,
474 where clearly identifiable onsets do not match the theoretical arrivals. In most cases, this is
475 due to an inaccurate velocity model.

476

477 In step 4, the velocity model is updated, based on the updated set of picks. We use the
478 program VELEST3.1 (Kissling et al., 1994), which simultaneously inverts for 1D P- and S-
479 wave velocities and hypocentral parameters. For this step, we concentrate on the picks of
480 events on or close to the CTF. This ensures good azimuthal coverage with a gap of less than
481 180° . Also, regional heterogeneities are likely to distort a uniform velocity model if the area
482 is chosen too large and diverse. We limit the selection further to events with an RMS of less
483 than 1.2, a minimum number of P-picks of 5, and a minimum number of S picks of 3.

484

485 Steps 2, 3 and 4 are run iteratively until the model and arrival time picks stabilise. Here, three
486 iterations proved to be sufficient.

487

488 **References**

489 Abercrombie, R. E. (1996). The magnitude-frequency distribution of earthquakes recorded
490 with deep seismometers at Cajon Pass, southern California. *Tectonophysics*, 261(1-3), 1-7.
491 DOI: 10.1016/0040-1951(96)00052-2.

492

493 Abercrombie, R. E., & Ekström, G. (2001). Earthquake slip on oceanic transform faults.
494 *Nature*, 410(6824), 74-77. DOI: 10.1038/35065064.

495

496 Agius, M. R., N. Harmon, C. A. Rychert, S. Tharimena, and J. M. M. Kendall (2018),
497 Sediment characterization at the equatorial Mid-Atlantic Ridge from P-to-S teleseismic phase
498 conversions recorded on the PI-LAB experiment, *Geophys. Res. Lett.*, 45, 12,244–12,252.
499 DOI: 10.1029/2018GL080565.

500

501 Amante, C., & Eakins, B. W. (2009). ETOPO1 arc-minute global relief model: procedures,
502 data sources and analysis. DOI: 10.7289/V5C8276M.

503

504 Bakun, W. H., & Joyner, W. B. (1984). The M_L scale in central California. *Bulletin of the*
505 *Seismological Society of America*, 74(5), 1827-1843. DOI: 10.1785/BSSA0740051827

506

507 Baumbach, M., Bindi, D., Grosser, H., Milkereit, C., Parolai, S., Wang, R., ... & Zschau, J.
508 (2003). Calibration of an ML scale in northwestern Turkey from 1999 Izmit aftershocks.

509 *Bulletin of the Seismological Society of America*, 93(5), 2289-2295. DOI:

510 10.1785/0120020157

511

512 Bird, P. (2003). An updated digital model of plate boundaries. *Geochemistry, Geophysics,*
513 *Geosystems*, 4(3). DOI: 10.1029/2001GC000252
514

515 Boettcher, M. S., Hirth, G., & Evans, B. (2007). Olivine friction at the base of oceanic
516 seismogenic zones. *Journal of Geophysical Research: Solid Earth*, 112(B1). DOI:
517 10.1029/2006JB004301
518

519 Boettcher, M. S., & Jordan, T. H. (2004). Earthquake scaling relations for mid-ocean ridge
520 transform faults. *Journal of Geophysical Research: Solid Earth*, 109(B12). DOI:
521 10.1029/2004JB003110
522

523 Bogiatzis, P., Karamitrou, A., Ward Neale, J., Harmon, N., Rychert, C. A., & Srokosz, M.
524 (2020). Source regions of infragravity waves recorded at the bottom of the equatorial Atlantic
525 Ocean, using OBS of the PI-LAB experiment. *Journal of Geophysical Research: Oceans*,
526 125(6), e2019JC015430. DOI: 10.1029/2019JC015430
527

528 Bonatti, E., Ligi, M., Gasperini, L., Peyve, A., Raznitsin, Y. U., & Chen, Y. J. (1994).
529 Transform migration and vertical tectonics at the Romanche fracture zone, equatorial
530 Atlantic. *Journal of Geophysical Research: Solid Earth*, 99(B11), 21779-21802. DOI:
531 10.1029/94JB01178
532

533 Braunmiller, J., & Nábělek, J. (2008). Segmentation of the Blanco Transform Fault Zone
534 from earthquake analysis: Complex tectonics of an oceanic transform fault. *Journal of*
535 *Geophysical Research: Solid Earth*, 113(B7). DOI: 10.1029/2007JB005213
536

537 Christeson, G. L., J. A. Goff, and R. S. Reece (2019), Synthesis of Oceanic Crustal Structure
538 From Two-Dimensional Seismic Profiles, *Reviews of Geophysics*, 57(2), 504-529.
539 DOI:10.1029/2019RG000641.
540

541 DeMets, C., Gordon, R. G., Argus, D. F., & Stein, S. (1994). Effect of recent revisions to the
542 geomagnetic reversal time scale on estimates of current plate motions. *Geophysical research*
543 *letters*, 21(20), 2191-2194. DOI: 10.1029/94GL02118
544

545 Dziewonski, A. M., T.-A. Chou and J. H. Woodhouse, Determination of earthquake source
546 parameters from waveform data for studies of global and regional seismicity, *J. Geophys.*
547 *Res.*, 86, 2825-2852, 1981. DOI:10.1029/JB086iB04p02825
548

549 Ekström, G., M. Nettles, and A. M. Dziewonski, The global CMT project 2004-2010:
550 Centroid-moment tensors for 13,017 earthquakes, *Phys. Earth Planet. Inter.*, 200-201, 1-9,
551 2012. DOI:10.1016/j.pepi.2012.04.002
552

553 Fox, P. J., & Gallo, D. G. (1984). A tectonic model for ridge-transform-ridge plate
554 boundaries: Implications for the structure of oceanic lithosphere. *Tectonophysics*, 104(3-4),
555 205-242. DOI: 10.1016/0040-1951(84)90124-0
556

557 Góngora, E., Carrilho, F., & Oliveira, C. S. (2004). Calibration of local magnitude ML in the
558 Azores archipelago based on recent digital recordings. *Pure and Applied Geophysics*, 161(3),
559 647-659. DOI: 10.1007/s00024-003-2467-0
560

561 Gregory, E. P., Singh, S. C., Marjanović, M., & Wang, Z. (2021). Serpentinized peridotite
562 versus thick mafic crust at the Romanche oceanic transform fault. *Geology*, 49(9), 1132-
563 1136. DOI: 10.1130/G49097.1
564
565 Gutenberg, B. and Richter, C.E, 1944. Frequency of earthquakes in California. *Bull. Seismol.*
566 *Soc. Am.*, 34: 185-188. DOI: 10.1785/BSSA0340040185
567
568 Harmon, N., Rychert, C., Agius, M., Tharimena, S., Le Bas, T., Kendall, J. M., & Constable,
569 S. (2018). Marine geophysical investigation of the chain fracture zone in the Equatorial
570 Atlantic from the PI²LAB experiment. *Journal of Geophysical Research: Solid Earth*,
571 123(12), 11-016. DOI: 10.1029/2018JB015982.
572
573 Harmon, N., C. A. Rychert, J. M. Kendall, M. Agius, P. Bogiatzis, and S. Tharimena (2020),
574 Evolution of the oceanic lithosphere in the equatorial Atlantic from Rayleigh wave
575 tomography, evidence for small-scale convection from the PI²LAB experiment, *Geochem.*
576 *Geophys. Geosys.*, 21, e2020GC009174.
577
578 Heimann, S., Isken, M., Kühn, D., Sudhaus, H., Steinberg, A., Daout, S., Cesca, S., Bathke,
579 H., Dahm, T. (2018). *Grond*: a probabilistic earthquake source inversion framework,
580 Potsdam: GFZ Data Services. DOI:10.5880/GFZ.2.1.2018.003
581
582 Hicks, S. P., Rietbrock, A., Ryder, I. M., Lee, C. S., & Miller, M. (2014). Anatomy of a
583 megathrust: The 2010 M8.8 Maule, Chile earthquake rupture zone imaged using seismic
584 tomography. *Earth and Planetary Science Letters*, 405, 142-155. DOI:
585 10.1016/j.epsl.2014.08.028.

586

587 Hicks, S. P., Okuwaki, R., Steinberg, A., Rychert, C. A., Harmon, N., Abercrombie, R. E., ...
588 & Sudhaus, H. (2020). Back-propagating supershear rupture in the 2016 M_w 7.1 Romanche
589 transform fault earthquake. *Nature Geoscience*, 13(9), 647-653. DOI: 10.1038/s41561-020-
590 0619-9

591

592 Hutton, L. K., & Boore, D. M. (1987). The M_L scale in southern California. *Bulletin of the*
593 *Seismological Society of America*, 77(6), 2074-2094. DOI: 10.1785/BSSA0770062074

594

595 Illsley-Kemp, F., Keir, D., Bull, J. M., Ayele, A., Hammond, J. O., Kendall, J. M., ... &
596 Goitom, B. (2017). Local earthquake magnitude scale and b -value for the Danakil region of
597 northern Afar. *Bulletin of the Seismological Society of America*, 107(2), 521-531. DOI:
598 10.1785/0120150253.

599

600 Kennett, B.L.N. Engdahl, E.R. & Buland R., 1995. Constraints on seismic velocities in the
601 Earth from travel times, *Geophys J Int*, 122, 108-124. DOI: 10.1111/j.1365-
602 246X.1995.tb03540.x.

603

604 Kissling, E., W.L. Ellsworth, D. Eberhart-Phillips, and U. Kradolfer (1994). Initial reference
605 models in local earthquake tomography, *J. Geophys. Res.*, 99, 19635-19646. DOI:
606 10.1029/93JB03138

607

608 Kohli, A., Wolfson-Schwehr, M., Prigent, C., & Warren, J. M. (2021). Oceanic transform
609 fault seismicity and slip mode influenced by seawater infiltration. *Nature Geoscience*, 14(8),
610 606-611. DOI: 10.1038/s41561-021-00778-1

611

612 Kuna, V. M., Nábělek, J. L., & Braunmiller, J. (2019). Mode of slip and crust–mantle
613 interaction at oceanic transform faults. *Nature Geoscience*, 12(2), 138-142. DOI:
614 10.1038/s41561-018-0287-1

615

616 Langston, C. A., Brazier, R., Nyblade, A. A., & Owens, T. J. (1998). Local magnitude scale
617 and seismicity rate for Tanzania, East Africa. *Bulletin of the Seismological Society of*
618 *America*, 88(3), 712-721. DOI: 10.1785/BSSA0880030712

619

620 Laske, G., Masters, G., Ma, Z. and Pasyanos, M., Update on CRUST1.0 – A 1-degree Global
621 Model of Earth's Crust, *Geophys. Res. Abstracts*, 15, Abstract EGU2013-2658, 2013.

622

623 Leptokaropoulos, K., Harmon, N., Hicks, S. P., Rychert, C. A., Schlaphorst, D., & Kendall, J.
624 M. (2021). Tidal Triggering of Microseismicity at the Equatorial Mid-Atlantic Ridge,
625 Inferred From the PI-LAB Experiment. *Journal of Geophysical Research: Solid Earth*,
626 126(9), e2021JB022251. DOI: 10.1029/2021JB022251

627

628 Lomax, A., J. Virieux, P. Volant and C. Berge, (2000), Probabilistic earthquake location in
629 3D and layered models: Introduction of a Metropolis-Gibbs method and comparison with
630 linear locations, in *Advances in Seismic Event Location*, Thurber, C.H., and N. Rabinowitz
631 (eds.), Kluwer, Amsterdam, 101-134. DOI: 10.1007/978-94-015-9536-0_5

632

633 Maia, M., Sichel, S., Briais, A., Brunelli, D., Ligi, M., Ferreira, N., ... & Oliveira, P. (2016).
634 Extreme mantle uplift and exhumation along a transpressive transform fault. *Nature*
635 *Geoscience*, 9(8), 619-623. DOI: 10.1038/ngeo2759

636

637 McGuire, J. J., Collins, J. A., Gouédard, P., Roland, E., Lizarralde, D., Boettcher, M. S., ... &

638 Van Der Hilst, R. D. (2012). Variations in earthquake rupture properties along the Gofar

639 transform fault, East Pacific Rise. *Nature Geoscience*, 5(5), 336-341. DOI:

640 10.1038/ngeo1454

641

642 Molnar, P. (2020). The brittle–plastic transition, earthquakes, temperatures, and strain rates.

643 *Journal of Geophysical Research: Solid Earth*, 125(7), e2019JB019335. DOI:

644

645 Morgan, J. P., & Parmentier, E. M. (1984). Lithospheric stress near a ridge–transform

646 intersection. *Geophysical Research Letters*, 11(2), 113-116. DOI: 10.1029/GL011i002p00113

647

648 Müller, R. D., Sdrolias, M., Gaina, C., & Roest, W. R. (2008). Age, spreading rates, and

649 spreading asymmetry of the world's ocean crust. *Geochemistry, Geophysics, Geosystems*,

650 9(4). DOI: 10.1029/2007GC001743.

651

652 Ottemöller, L., & Sargeant, S. (2013). A local magnitude scale ML for the United Kingdom.

653 *Bulletin of the Seismological Society of America*, 103(5), 2884-2893. DOI:

654 10.1785/0120130085

655

656 Parmentier, E. M., & Morgan, J. P. (1990). Spreading rate dependence of three-dimensional

657 structure in oceanic spreading centres. *Nature*, 348(6299), 325-328. DOI: 10.1038/348325a0

658

659 Richter, C. F. (1935). An instrumental earthquake magnitude scale, *Bull. Seism. Soc. Am.* 25,

660 1-31. DOI: 10.1785/BSSA0250010001

661

662 Richter, C. F. (1958). *Elementary Seismology*, W. H. Freeman and Co., San Francisco,
663 California, 578 pp.

664

665 Roland, E., Behn, M. D., & Hirth, G. (2010). Thermal–mechanical behavior of oceanic
666 transform faults: Implications for the spatial distribution of seismicity. *Geochemistry,
667 Geophysics, Geosystems*, 11(7). DOI: 10.1029/2010GC003034

668

669 Rychert, C. A., Tharimena, S., Harmon, N., Wang, S., Constable, S., Kendall, J. M., ... &
670 Schlaphorst, D. (2021). A dynamic lithosphere–asthenosphere boundary near the equatorial
671 Mid-Atlantic Ridge. *Earth and Planetary Science Letters*, 566, 116949. DOI:
672 10.1016/j.epsl.2021.116949

673

674 Saikia, U., C. Rychert, N. Harmon and J.M. Kendall (2020), Sediment structure at the
675 equatorial mid atlantic ridge constrained by seafloor admittance using data from the PI LAB
676 experiment, *Mar. Geophys. Res.*, 41, 3, doi: 10.1007/s11001-020-09402-0

677

678 Saikia, U., C. Rychert, N. Harmon, and J. M. Kendall (2021), Upper mantle anisotropic shear
679 velocity structure at the equatorial Mid-Atlantic ridge constrained by Rayleigh wave group
680 velocity analysis from the PI-LAB experiment, *Geochem. Geophys. Geosys.*, 22,
681 e2020GC009495, DOI: 10.1029/2020GC009495

682

683 Saunders, I., Ottemöller, L., Brandt, M. B., & Fourie, C. J. (2013). Calibration of an ML
684 scale for South Africa using tectonic earthquake data recorded by the South African National

685 Seismograph Network: 2006 to 2009. *Journal of seismology*, 17(2), 437-451. DOI:
686 10.1007/s10950-012-9329-0
687
688 Schlaphorst, D., Kendall, J. M., Collier, J. S., Verdon, J. P., Blundy, J., Baptie, B., ... &
689 Bouin, M. P. (2016). Water, oceanic fracture zones and the lubrication of subducting plate
690 boundaries—insights from seismicity. *Geophysical Journal International*, 204(3), 1405-1420.
691 DOI: 10.1093/gji/ggv509.
692
693 Schorlemmer, D., Wiemer, S., & Wyss, M. (2005). Variations in earthquake-size distribution
694 across different stress regimes. *Nature*, 437(7058), 539-542. DOI: 10.1038/nature04094.
695
696 Shi, P., Meng W. & Pockalny, R. The ubiquitous creeping segments on oceanic transform
697 faults, *Geology* 50, 199-204 (2021). DOI: 10.1130/G49562.1
698
699 Slemmons, D. B., & Depolo, C. M. (1986). Evaluation of active faulting and associated
700 hazards. *Active Tectonics*, 1986, 45-62.
701
702 Tarantola, A. and Valette, B., 1982, Inverse problems = quest for information., *J. Geophys.*,
703 50, 159-170.
704
705 Wang, S., Constable, S., Rychert, C. A., & Harmon, N. (2020). A lithosphere–asthenosphere
706 boundary and partial melt estimated using marine magnetotelluric data at the central Middle
707 Atlantic Ridge. *Geochemistry, Geophysics, Geosystems*, 21(9), e2020GC009177. DOI:
708 10.1029/2020GC009177
709

710 Wessel, P., W. H. F. Smith, R. Scharroo, J. Luis, and F. Wobbe, Generic Mapping Tools:
711 Improved Version Released, EOS Trans. AGU, 94(45), p. 409–410, 2013.
712 DOI:10.1002/2013EO450001.

713

714 Yu, Z., Singh, S. C., Gregory, E. P., Maia, M., Wang, Z., & Brunelli, D. (2021). Semibrittle
715 seismic deformation in high-temperature mantle mylonite shear zone along the Romanche
716 transform fault. *Science Advances*, 7(15), eabf3388. DOI: 10.1126/sciadv.abf3388

717

718 Yue, H., T. Lay, and K. D. Koper (2012), En échelon and orthogonal fault ruptures of the 11
719 April 2012 great intraplate earthquakes, *Nature*, 490(7419), 245-249.
720 DOI:10.1038/nature11492.

721

722 **Tables**

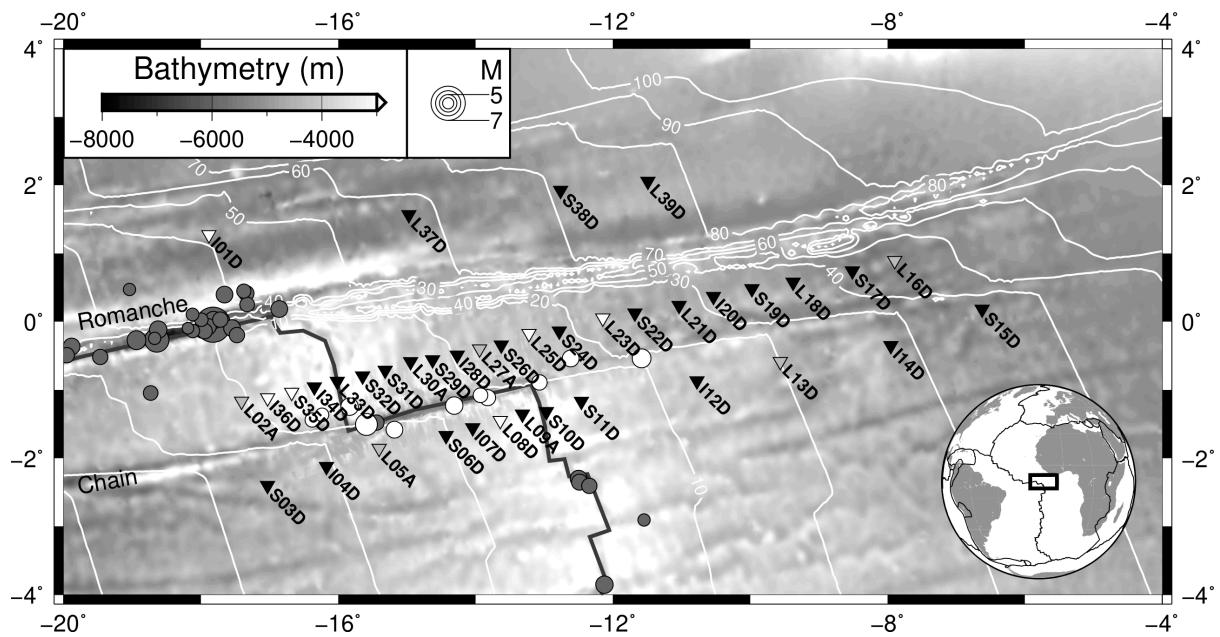
723 Tab. 1: PI-LAB network OBS station details. Stations indicated with an asterisk were not
 724 used. Except for L27A running time is equivalent to deployment time.

725

726	Station	Lon	Lat	Depth (m)	Running Time	Notes
727	I01D*	-17.8855	1.2734	-4047	N/A	<i>unrecovered</i>
728	L02A	-17.4085	-1.1667	-3499	06/03/2016 – 24/03/2017	<i>did not level</i>
729	S03D	-17.0315	-2.4021	-3750	05/03/2016 – 25/03/2017	
730	I04D	-16.1733	-2.1238	-3928	07/03/2016 – 24/03/2017	
731	L05A	-15.4058	-1.8577	-4052	07/03/2016 – 21/03/2017	<i>stopped after 150 days</i>
732	S06D	-14.4298	-1.6703	-3778	06/03/2016 – 19/03/2017	
733	I07D	-14.0428	-1.5565	-3819	08/03/2016 – 22/03/2017	
734	L08D*	-13.6409	-1.4493	-3357	08/03/2022 – 18/03/2017	<i>only 1 horizontal channel</i>
735	L09A	-13.3185	-1.3569	-3378	08/03/2016 – 18/03/2017	<i>1 flat horizontal channel</i>
736	S10D	-12.9697	-1.3180	-3015	07/03/2016 – 18/03/2017	
737	S11D	-12.4602	-1.1691	-2905	07/03/2016 – 18/03/2017	
738	I12D	-10.7766	-0.8683	-4022	19/03/2016 – 17/03/2017	
739	L13D	-9.5619	-0.5862	-4659	09/03/2016 – 16/03/2017	<i>usable data until 23/12/16</i>
740	I14D	-7.9524	-0.3522	-4702	10/03/2016 – 10/03/2017	
741	S15D	-6.6228	0.1814	-4927	09/03/2016 – 16/03/2017	<i>rocking, some bad data</i>
742	L16D	-7.8953	0.8933	-4581	11/03/2016 – 15/03/2017	<i>usable data until 24/02/16</i>
743	S17D	-8.5121	0.7422	-5205	09/03/2016 – 15/03/2017	
744	L18D	-9.3765	0.5769	-4890	11/03/2016 – 14/03/2017	
745	S19D	-9.9754	0.4809	-4607	10/03/2016 – 14/03/2017	
746	I20D	-10.5352	0.3681	-4724	12/03/2016 – 13/03/2017	
747	L21D	-11.0380	0.2364	-4625	11/03/2016 – 13/03/2017	
748	S22D	-11.6799	0.1254	-4352	10/03/2016 – 13/03/2017	
749	L23D*	-12.1478	0.0521	-4631	12/03/2016 – 12/03/2017	<i>timing issues</i>
750	S24D	-12.7806	-0.1383	-4453	10/03/2016 – 13/03/2017	
751	L25D*	-13.2230	-0.1745	-4207	12/03/2022 – 11/03/2017	<i>disk failure</i>
752	S26D	-13.6260	-0.3434	-4216	11/03/2016 – 12/03/2017	
753	L27A*	-13.9427	-0.4007	-3928	12/03/2016 – 23/08/2016	<i>1 flat horizontal channel</i>
754	I28D	-14.2684	-0.4918	-3711	13/03/2016 – 11/03/2017	
755	S29D	-14.6272	-0.5597	-3626	11/03/2016 – 11/03/2017	
756	L30A	-14.9467	-0.5880	-4003	13/03/2016 – 10/03/2017	
757	S31D	-15.3188	-0.7141	-3408	11/03/2016 – 11/03/2017	
758	S32D	-15.6470	-0.7968	-2967	11/03/2016 – 11/03/2017	
759	L33D	-16.0152	-0.8747	-3919	13/03/2016 – 09/03/2017	
760	I34D	-16.3485	-0.9579	-2964	14/03/2016 – 09/03/2017	
761	S35D*	-16.6798	-1.0372	-3773	11/03/2016 – 11/03/2017	<i>disk failure</i>
762	I36D*	-17.0306	-1.1170	-3938	N/A	<i>unrecovered</i>
763	L37D	-14.9718	1.5657	-5054	19/03/2016 – 08/03/2017	
764	S38D	-12.7623	1.9218	-4926	18/03/2016 – 08/03/2017	
765	L39D*	-11.4904	2.0557	-4685	20/03/2016 – 07/03/2017	<i>unrecovered</i>

766
767

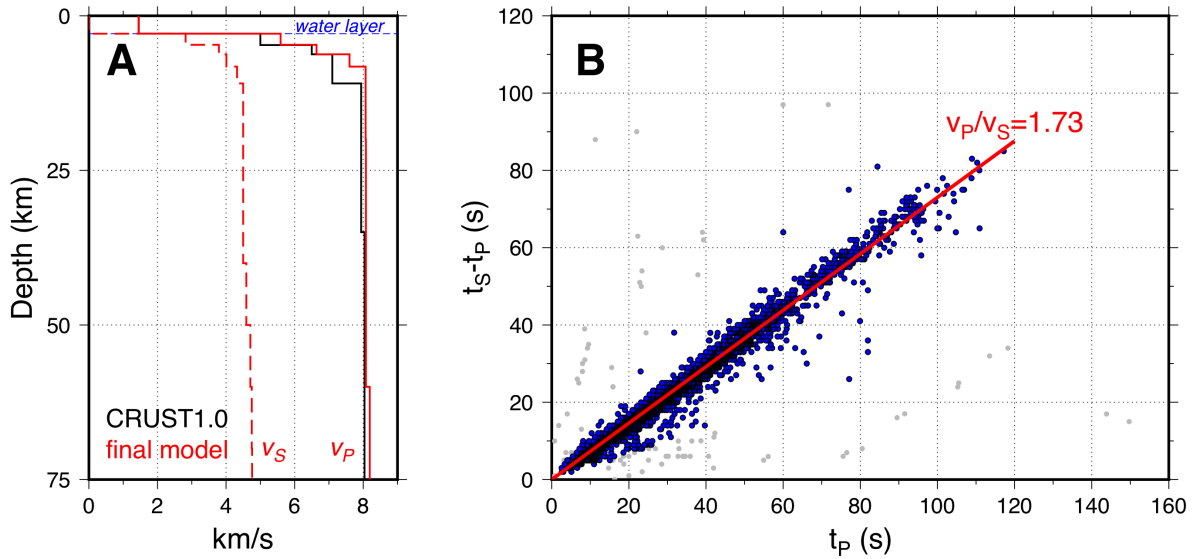
768 **Figures**



769

770 Fig. 1: Map of the study area (see inset for global context), including the PI-LAB station
 771 network. Some stations did not provide usable data for the entire timespan of the experiment
 772 (white triangles), some stations were only returning useful data for parts of the deployment
 773 (grey triangles); see details in Table 1. Events from the ISC during the time of the
 774 deployment are shown by circles, events around the CTF (white circles) have been used to
 775 calibrate the local event magnitude (see Fig. 3). In the global catalogue, all of these events
 776 have been assigned default depth values of 10km. Bathymetry data is taken from ETOPO1
 777 (Amante & Eakins, 2009) with an additional higher resolution image around the CTF
 778 (Harmon et al., 2018). The thick solid line denotes the MAR location (adapted from Bird,
 779 2003). White thin lines show age contours in Ma (Müller et al, 2008).

780



781

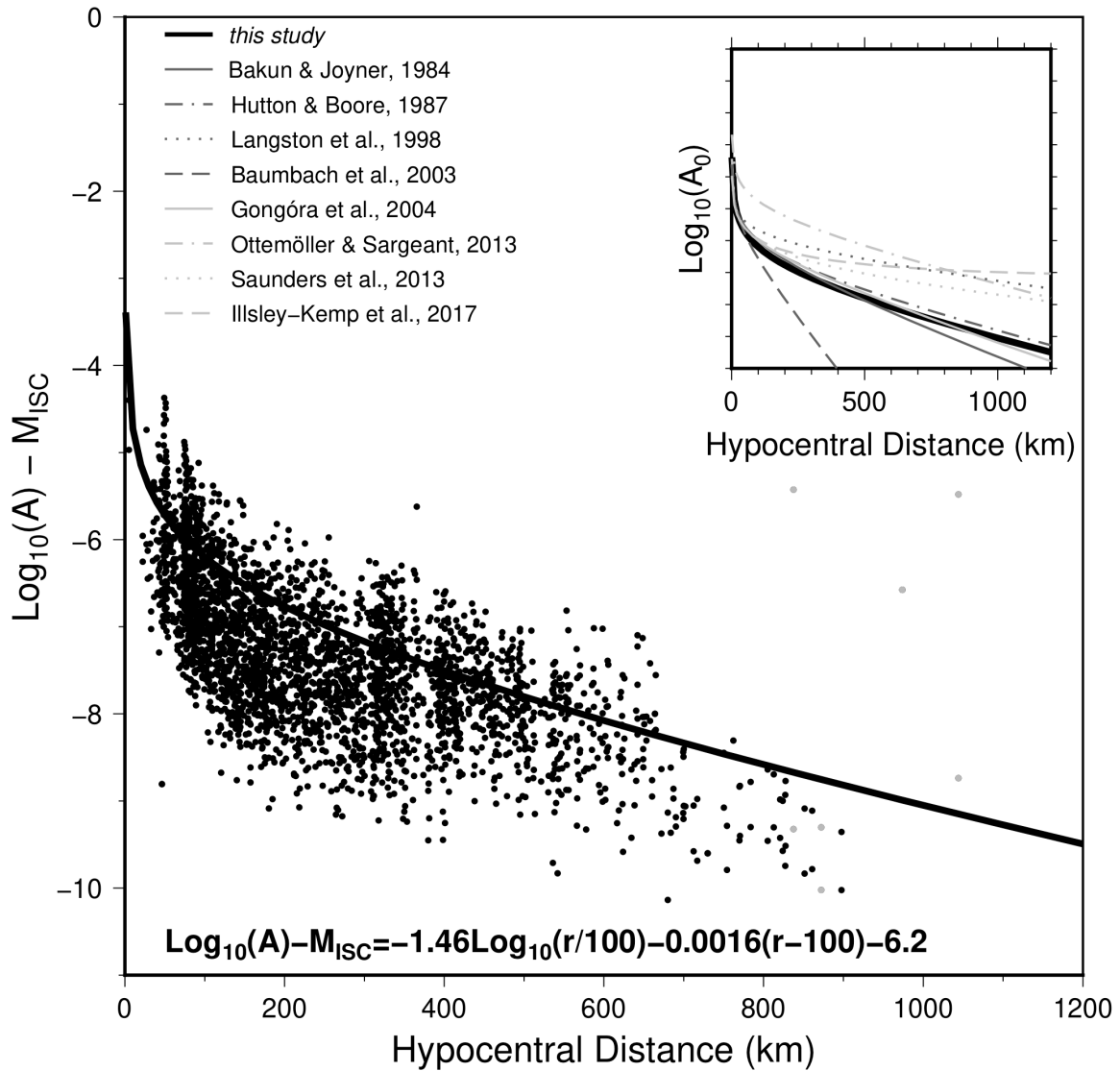
782 Fig. 2: (A) Initial (CRUST1.0) and final 1-D velocity-depth models. Note that CRUST1.0

783 only provides a P-velocity model. (B) Wadati plot of P- and S- arrival time picks (7345 pairs)

784 for all events. The red line shows the average v_P/v_S value of 1.73. About 98.1% (7206 pairs in

785 blue) fall within ± 0.4 of that value, about 83.7% (6146 pairs) fall within ± 0.1 .

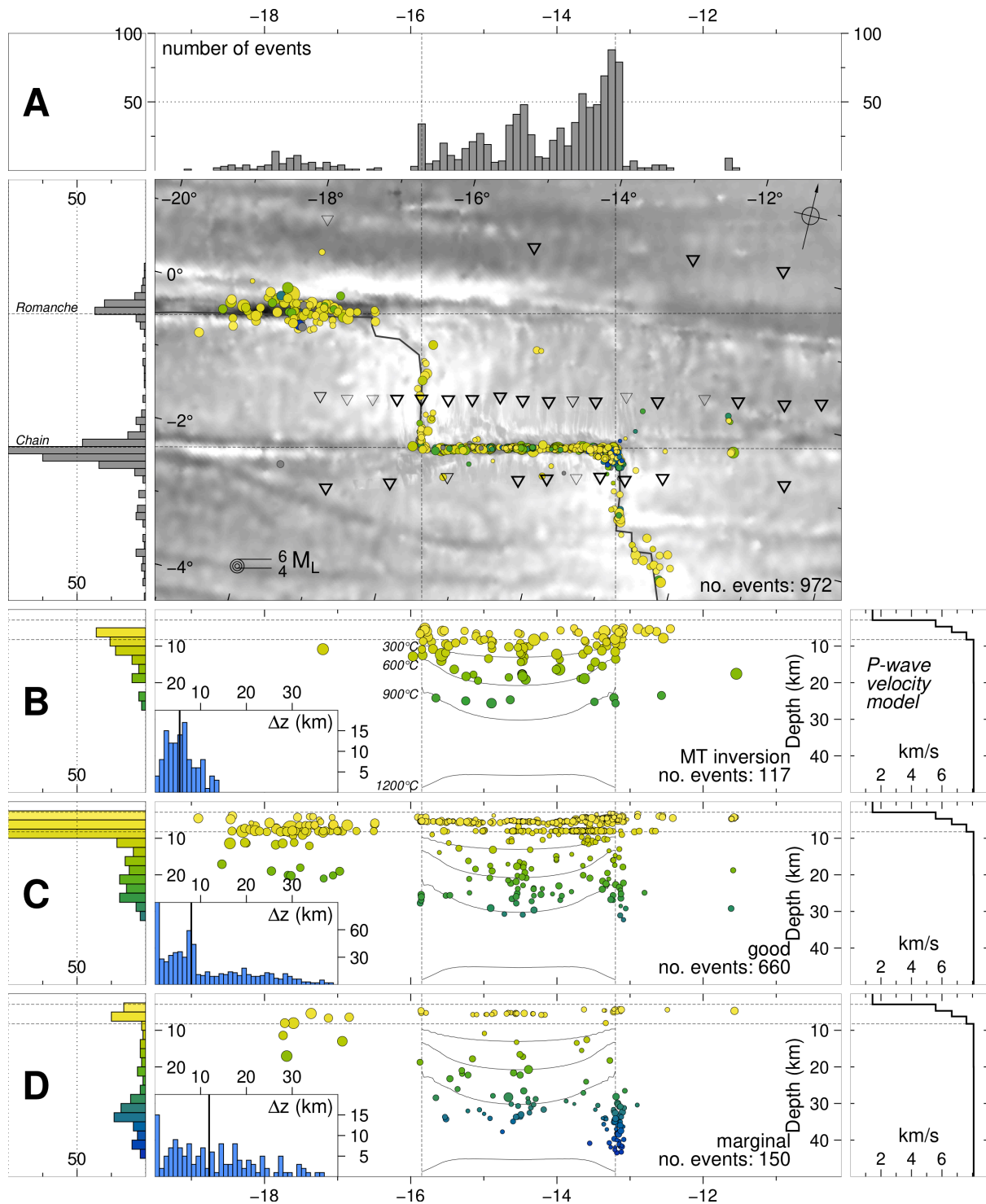
786



787

788 Fig. 3: Magnitude calibration with MT inversion solutions. Note, that results from station
 789 S15D (grey dots) are taken out of the calculation, since the instrument was located on a slope
 790 rocking and produced erroneous data. The inset shows different correction curves, all shifted
 791 to match the original setup by Richter (1935, 1958).

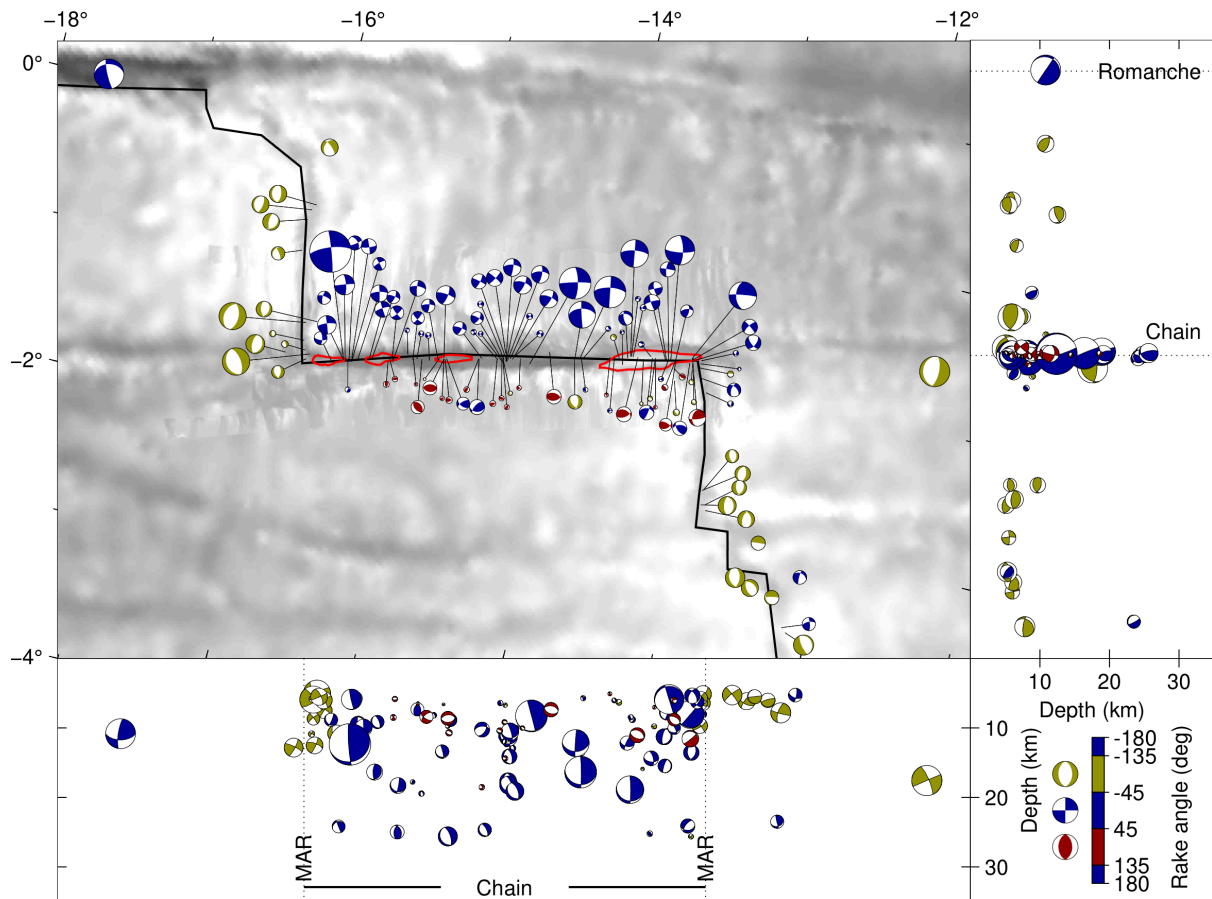
792



793

794 Fig. 4: Catalogue event location and magnitude results. (A) Map showing the epicentres
 795 coloured by depth. Top and left panels show histograms by projected longitude and latitude.
 796 (B-D) Cross section along the CTF and FZ. Depth uncertainties are shown in the blue
 797 histograms with the median value being depicted by vertical black lines. For clarity, error
 798 bars have been omitted from the figure but can be seen in Supplementary Figure S4. Events

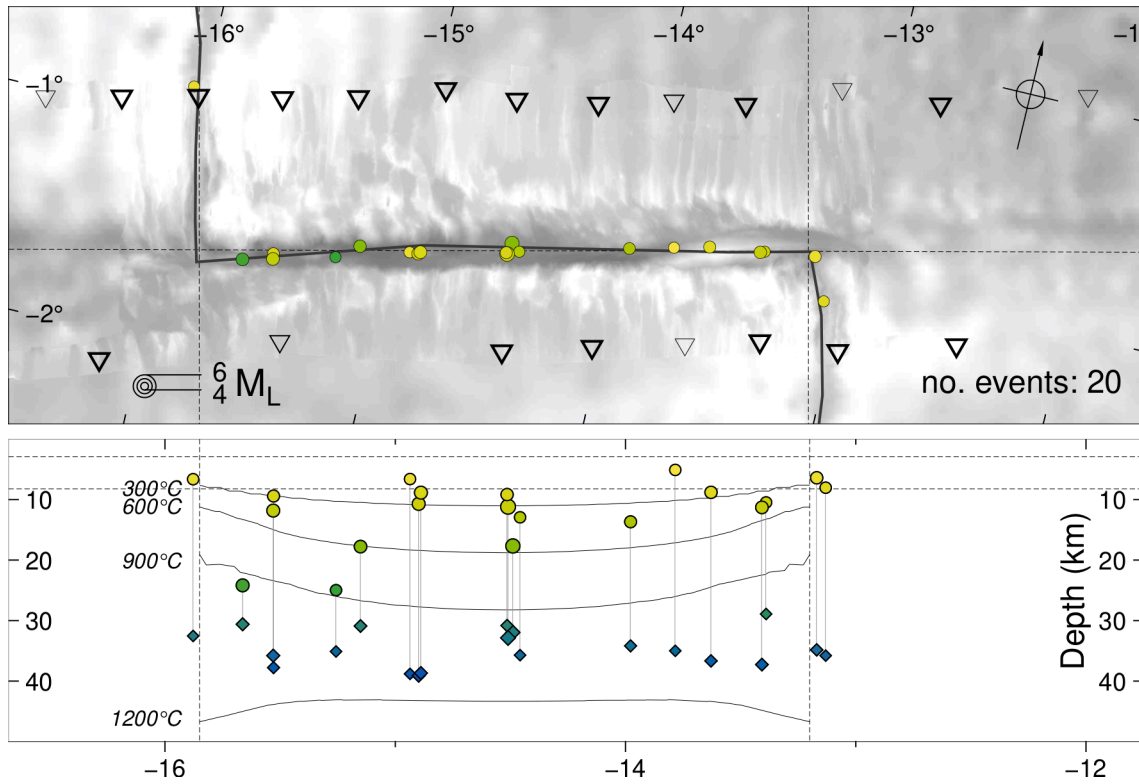
799 are divided by quality (B: events for which moment tensor inversion was possible; C: good
800 locating results with NonLinLoc; D: marginal locating results with NonLinLoc) Isotherms
801 (300 – 1200°C in steps of 300°C) from a half space cooling model (using the lower half
802 spreading rate from the African plate, 15.7mm/yr, which results in deeper isotherms) are also
803 shown along the CTF. Also shown are depth histograms (left) and the final P-velocity model
804 (right). See Figure 1 for further details. See Supplementary Table S1 for event details.
805



806

807 Fig. 5: Map including all focal mechanisms (shown as MT inversion results in Fig. 4). The
 808 mechanisms are placed apart from the OTF for better visibility. The shading is based on their
 809 dominant mechanism according to rake angle. Red lines indicate mapped transpressive
 810 flower-structures on the CTF (Harmon et al., 2018). See Figure 1 for further details. See
 811 Supplementary Table S2 for focal mechanism details. See Supplementary Figure S5 for an
 812 example of a waveform fit.

813



814

815 Fig. 6: Map showing all MT results that show a bimodal distribution with good shallow and
 816 deep solutions, including shallow (circles) and deep (diamonds) in the cross section.